



# Micro-Raman Spectroscopy Explains the Population-Scale Heterogeneity in Lipid Profile in *Chlamydomonas reinhardtii* Cultivated Under Single-Stage and Two-Stage Salt Stress

Shubhangi Pandey<sup>1</sup> · Sandhya Mishra<sup>2</sup> · G. Archana<sup>1</sup> · Debjani Bagchi<sup>3</sup>

Received: 21 November 2023 / Accepted: 21 August 2024

© The Author(s), under exclusive licence to Springer Science+Business Media, LLC, part of Springer Nature 2024

## Abstract

Salt stress on green microalgae increases lipid production at the cost of cellular homeostasis. Rapid optimization of growth conditions for high lipid productivity and biomass yield is crucial for translation to industrial-scale biodiesel production. To achieve this, the present study has developed a spectroscopic non-invasive analysis of lipid molecules produced by *Chlamydomonas reinhardtii* in two-stage salt stress, wherein 100 mM NaCl was added at two different time points: day 2 (D2 100) and day 4 (D4 100) of growth. Two-stage stress resulted in cell morphology like the photoautotrophic control grown in normal conditions, with negligible palmelloid formation in contrast to single-stage. Raman spectra acquired from ~30 individual cells in each culture revealed heterogeneities in lipid composition. Discrete wavelet transform decomposition of the Raman signal was used to enhance the signal-to-noise ratio and accuracy of Raman peak center estimation. An overall increase in heterogeneity indices for fatty acid degree of unsaturation was observed under two-stage salt stress: fourfold for D2 100 and ninefold for D4 100, especially at the stationary growth phase. The ratio of the CH<sub>2</sub>/CH<sub>3</sub> scissoring mode (1440 cm<sup>-1</sup>) and the C=O stretching mode (1750 cm<sup>-1</sup>) reveals the shortening of fatty acid chain length in D4 100. Although Raman bands of lipids formed in all growth conditions are on average like Triolein (18:1), analyses of the degree of unsaturation (1656/1440 cm<sup>-1</sup>) clarify the increased content of bi and tri-unsaturation only in D4 100. This non-invasive lipid profiling reveals that D4 100 is likely a non-ideal condition to obtain high-quality biodiesel-producing lipids. A comparative analysis of single-cell fluorescence microscopy of lipid droplets and Raman intensity of lipids shows the sensitivity of Raman intensity in deciphering the relative response of the cells to salt stress.

---

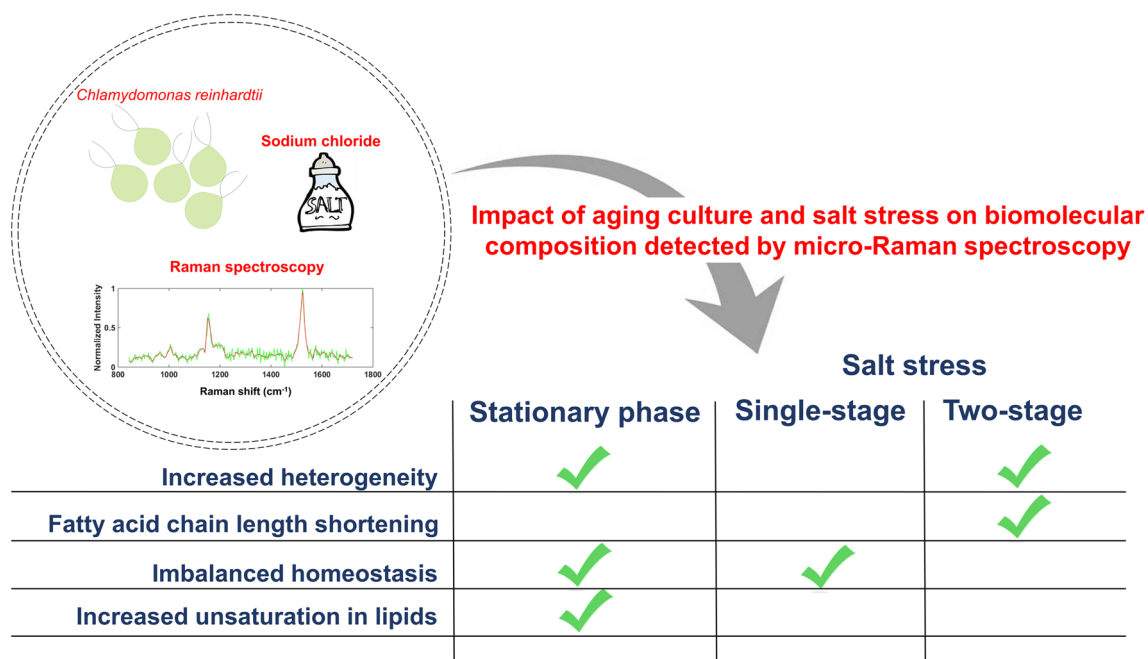
✉ Debjani Bagchi  
debjani.bagchi-phy@msubaroda.ac.in

<sup>1</sup> Department of Microbiology and Biotechnology Centre,  
Faculty of Science, The Maharaja Sayajirao University  
of Baroda, Vadodara, Gujarat, India

<sup>2</sup> Department of Applied Phycology and Biotechnology,  
CSIR–Central Salt & Marine Chemicals Research Institute  
(CSMCRI), Bhavnagar, Gujarat, India

<sup>3</sup> Department of Physics, Faculty of Science, The Maharaja  
Sayajirao University of Baroda, Vadodara, Gujarat, India

## Graphical Abstract



**Keywords** Lipid · Unsaturation · Chain length · Heterogeneity · Biodiesel · Microalgae · Homeostasis

## Introduction

Through efficient light-harvesting and carbon dioxide fixation mechanisms, microalgae have evolved as a promising source of energy feedstock, including biofuels, nutraceuticals, and other high-value products [1]. In the microalgal biofuel industry, the quantity and quality of the product are among the important factors that pose challenges in present times [2]. This concern exists despite numerous technological and genetic modification approaches for increasing the microalgal biomass yield and lipid productivity [3, 4]. Microalgae are known to produce higher amounts of biofuel-related compounds under environmental stress conditions such as limitation of nutrients including phosphorus and nitrogen, supra-optimal conditions of temperature, light, carbon dioxide, and salinity [5]. The current study is focused on reviewing the effects of salt stress on *Chlamydomonas reinhardtii*. Salt stress results in the loss of lipid productivity due to cell death and poor biomass [6]; hence, it demands a balanced trade-off to achieve maximum lipid production with good biomass yield. Several innovative strategies have been employed to maximize biomass and lipid (triacylglycerol) yields under stress conditions [7], for instance, changing the mode of cultivation from continuous to batch culture in *Acutodesmus obliquus* under nitrogen starvation led to higher triacylglycerol yields [8]. Recently, two-stage

cultivation results in biomass accumulation in the first stage, followed by exposure to stress elements in the second stage. This benefits the net lipid content in microalgae [9]. Two-stage salt stress in *Chlamydomonas* sp. JSC4 increases the biomass accumulation and lipid content by nearly four times compared to single-stage [10].

Most of the studies use bulk measurement techniques like gas chromatography-based detection tools (GC-FID or GC-MS) for quantifying the lipid content and determining the lipid composition. Despite the usefulness of GC in lipid profiling, resource-extensive sample preparation steps involving efficient harvesting of microalgae and lipid extraction procedures render GC difficult to use for multivariable screening. Detailed lipid composition is essential to learning the biofuel potential of the microalgal lipids, which is primarily dictated by the degree of unsaturation, the basis of all the biofuel quality parameters [11]. Raman spectroscopy (RS) offers rapid, high-throughput, multivariate, and non-invasive analysis of lipid composition [12]. Raman spectroscopy when used in the confocal geometry (micro-RS) further permits the acquisition of high-resolution Raman scattering with just a few microliters of culture volume. Analysis of microalgal lipids obtained using RS as well as micro-RS has also been validated well by correlating the quantifications obtained from GC-MS [13, 14]. In the field of metabolomics, fast,

non-invasive metabolite fingerprinting has been possible using RS [15]. Micro-RS permits a label-free approach to simultaneously study multiple cellular metabolites and biomolecules such as starch, polysaccharides, proteins, lipids, carbohydrates, and carotenoids [14, 16, 17]. In the past decade, micro-RS has emerged as a rapid lipid profiling tool in microalgal research, especially at the single-cell level [18–20]. It even mitigates the problem of weak Raman signal, thus resulting in accurate localization and sensitive signal detection [21]. This approach of single-cell measurement allows tracking of the single-cell phenotypic variability to reveal useful information lost in bulk measurements, which observe the mean of a variable. For example, effects due to a bimodal distribution, a broad distribution, or the presence of significant states in the tails of a probability distribution get ignored in bulk measurements [22]. This distribution analysis has revealed the presence of antibiotic-resistant persister cells in the bacterial population which aids in biofilm formation [23]. Although heterogeneity is inherent in cells due to noise in gene expression levels [24], it holds the key to a better understanding of the response of an organism to changing environmental conditions. However, despite the industrial importance, there are very few studies that focus on characterizing heterogeneity and understanding the underlying distribution as a function of the stress in microalgae.

The objective of this study was to critically analyze the feasibility of using micro-Raman data to identify population-scale lipid compositional heterogeneities in *Chlamydomonas reinhardtii* cells when exposed to single-stage and two-stage salt stress and to predict the biofuel potential of lipids produced. The measurements were performed at different stages of microalgal growth to understand the impact of stress along with the life stages on the lipid profile of microalgae. This study likely serves to be the first of its kind to deliver such a detailed insight into the microalgal lipid heterogeneities as a function of salt stress and growth. The effect of stress on cellular stasis was also explored from the inter-relations of biomolecules. Some drawbacks of using micro-Raman spectroscopy, due to limited spectral resolution, low intensity, and non-uniform spatial distribution of biomolecules within a single cell, are also discussed in this paper. Nile red fluorescence measurements were used to analyze fluctuations in single-cell lipid accumulation in response to salinity stress. This is coupled with multivariate analysis of single-cell Raman data for improved discrimination of signal due to chemical composition differences. The present studies show that if suitable care is taken, micro-RS can successfully allow simultaneous, non-invasive, multivariate studies of cellular homeostasis, lipid production, leading to detection of population-scale heterogeneities in lipid composition, otherwise averaged out in bulk lipidomics.

## Experimental Section

### Microalgal Strain and Growth Conditions

*Chlamydomonas reinhardtii* CC-125 was procured from *Chlamydomonas* Resource Centre, Minnesota. Cells were cultivated in the standard medium called Tris–acetate-phosphate (TAP), at neutral pH 7.0 and a constant temperature of 25 °C. The microalgal culture was grown under constant shaking at 200 rpm, with a 12 h:12 h light to dark cycle using white light of  $\sim 50 \mu\text{mol photons m}^{-2} \text{s}^{-1}$  intensity in the presence of minimal antibiotic concentration of 40  $\mu\text{g/ml}$  ampicillin to avoid any bacterial contamination (adapted from previous studies [25, 26]). The growth of the culture was monitored at 680 nm ( $\text{OD}_{680}$ ) using a UV–visible spectrophotometer (UV-1800, Shimadzu). Cell density was determined from three independently grown cultures using the following equation:

$$\text{Cells} \left( \times \frac{10^6}{\text{ml}} \right) = 0.015 + 3.64 \times \text{OD}_{680} \quad (1)$$

This equation was derived from the cell count using a hemacytometer at different cell concentrations (Fig. S1) of *C. reinhardtii*.

### Cultivation of *C. reinhardtii* Under Salt Stress

Salt stress was provided to the microalgal culture using a final concentration of 100 mM sodium chloride, NaCl, as described in the previous study [27]. This concentration was selected based on the adverse effects of osmotic shock on the cells when a NaCl concentration higher than 100 mM was used (data not shown). The salt stress was provided in two ways: single-stage and two-stage as shown in Fig. 1. Briefly, the single-stage cultures had 100 mM NaCl added at the beginning of culturing (SS 100). The two-stage cultures had 100 mM NaCl added in the early-log phase on the 2nd day of the culture (D2 100) and in the mid-log phase on the 4th day of the culture (D4 100). The *C. reinhardtii* cells were harvested on the 6th day (D6) and 10th day (D10), at the end-log and stationary phase, respectively. The autotrophically grown *C. reinhardtii* under the optimum environmental conditions without any stress serves as the negative control in all the experiments.

### Single-Cell Micro-Raman Spectroscopy Measurements

For visualizing *C. reinhardtii* CC-125 cells under a microscope conjugated with Raman spectroscopy, 1 ml of the culture was centrifuged at 8000 *g* for 5 min and

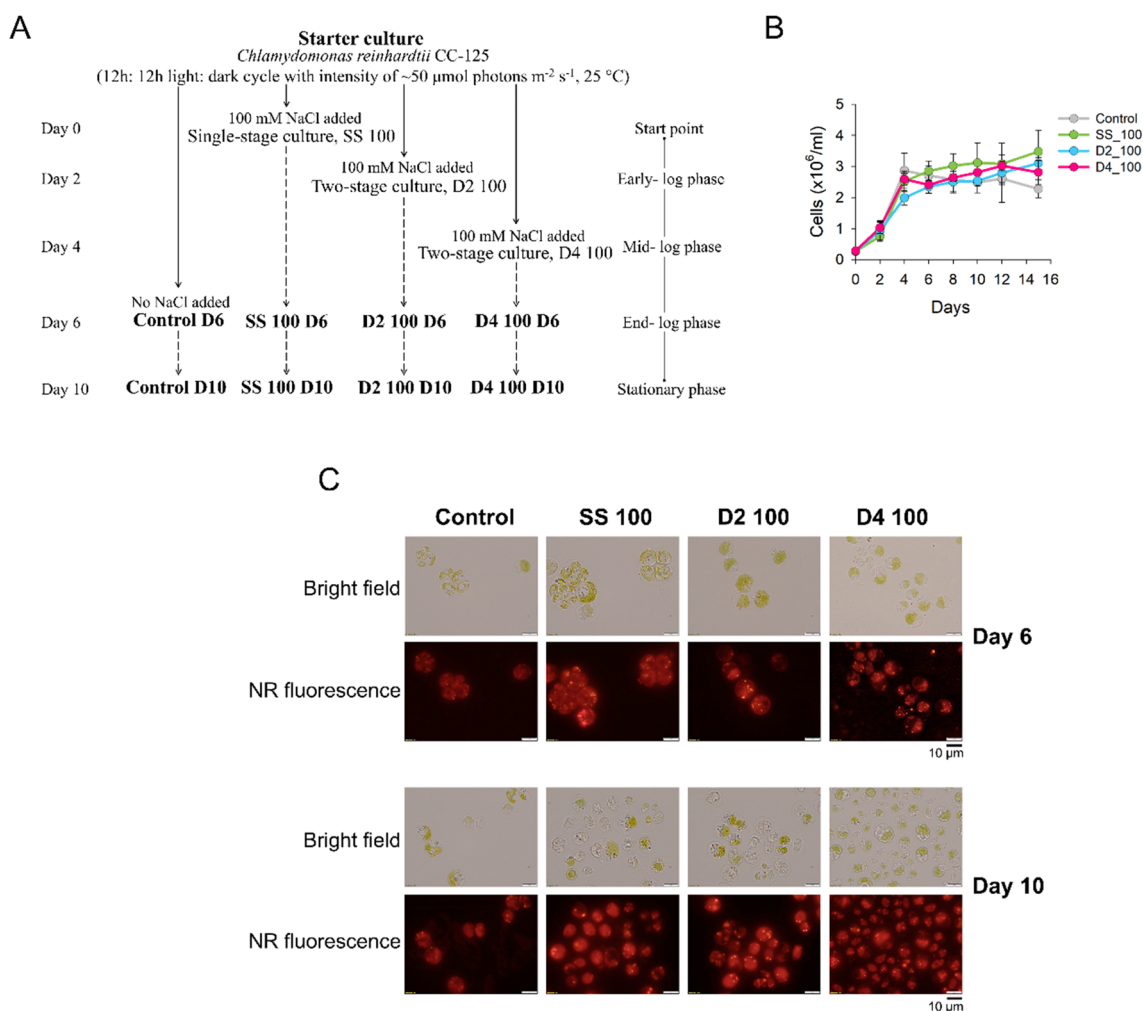


**Fig. 1** Methods of cultivation of *C. reinhardtii* under single-stage and two-stage salt stress and their effect on growth and morphology. **A** *C. reinhardtii* cells grown in normal TAP media without salt stress are referred to as control D6 and control D10, depending on the day of sampling, i.e., day 6 (D6) and day 10 (D10), respectively. Similarly, single-stage with 100 mM NaCl culture is referred to as SS 100 D6 and SS 100 D10; early-log phase salt stress cultures are D2 100 D6 and D2 100 D10; mid-log salt stress cultures are referred to as D4

100 D6 and D4 100 D10. **B** Growth curve depicting the change in the cell density of *C. reinhardtii* with time (in days). Data points represent the average for three independent experiments. **C** *C. reinhardtii* cells stained with Nile red dye were observed with epifluorescence microscopy (objective of  $\times 100$ , 1.4 N.A., scale bar = 10  $\mu\text{m}$ ). The green-colored pigments in the bright field images are the photosynthetic pigments, chlorophyll, and carotenoids. The Nile red fluorescence in the lower panel depicts the lipid droplet accumulation

concentrated into a wet paste, spotted on a clean glass slide, and dried in the air, as described by He *et. al* in 2017 [14]. Raman scattering experiments were carried out with a micro-Raman spectrometer (STR 300 series, AIRIX Corp., Japan) having an upright confocal geometry, as described previously [27]. The incident beam of 50 mW power, attenuated by 5% with a neutral density filter from a 532 nm diode-pumped solid-state laser (Laser Quantum), was passed through a  $\times 50$  objective lens (N.A. 0.6), and the back-scattered Raman signal was collected through this same objective. This geometry yielded a diffraction-limited focal spot of about 500 nm, resulting in a small focal volume. After elimination of the elastic Rayleigh scattered

light with a holographic filter, the Stokes scattered light was passed through a grating having a resolution of about  $2.4 \text{ cm}^{-1}$  in the fingerprint region, detected by an Andor iDus EMCCD, cooled to  $-70 \text{ }^\circ\text{C}$ . The acquisition time was optimized to 2 s to collect the scattered light from individual cells, maintaining near single-cell conditions. Two signals of 2 s duration each were then averaged, and the instrumental background was subtracted to yield the final signal. A total of  $\sim 30$  Raman spectra were captured from a single preparation of a culture. The spectrometer was calibrated using naphthalene as the standard before data acquisition.

## Signal Processing of Raman Spectra

Each Raman spectrum was first background subtracted and de-trended by subtracting a polynomial best representing the background by a non-linear least-square fitting algorithm. The Raman spectrum was first normalized to correct for the incident intensity fluctuations arising from the scattering or absorption of the incident light. The resultant data obtained after this pre-treatment had the same baselines and maximum peak intensity permitting a direct comparison of microalgal cells grown under different conditions. This pre-signal processing of the data was done using custom-made codes in MATLAB. The pre-treated data was then processed using the discrete wavelet transform (DWT) algorithm.

The DWT algorithm is a fast-hierarchical scheme that passes a signal with length  $L = 2^n$  data points through a series of consecutive low-pass and high-pass filters, which decompose the signal into different levels or frequency bands. Symlet 4 wavelet was used with a level 2 decomposition, which regulates the low-pass and high-pass filters. The low-pass filter outputs are referred to as approximation coefficients and the high-pass filter outputs are referred to as detail coefficients. The data was decimated after this filter step by a factor of two per the Nyquist theorem. Typical approximation coefficients from one of the Raman signals along with the two detail coefficients (non-decimated) as an outcome of this 2-level decomposition are shown in Fig. S2. To decompose a signal with an optimal decomposition criterion, a signal of length  $L = 2^n$  can be expanded in  $\alpha$  different ways, where  $\alpha \geq 2^{n/2}$  is the number of binary subtrees of a complete binary tree of depth  $L$ . Since  $\alpha$  is a large number, entropy-based (additive-type property) criterion, the classical Shannon entropy (non-normalized squared value of the logarithm of each signal sample) was found to be appropriate. The best wavelet decomposition tree was computed, and an appropriate threshold was selected for signal reconstruction. To obtain peak parameters, deconvolution was performed for the overlapping peaks both before and after DWT treatment from the Raman data and observed to yield better estimates of peak center values.

## Single-Cell Quantification of Neutral Lipids by Epifluorescence Microscopy of *C. reinhardtii* Cells

Nile red staining of the neutral lipids, triacylglycerols (TAGs), in *C. reinhardtii* cells, was carried out by incubating the microalgal cells with the final concentration of 1  $\mu\text{g}/\text{ml}$  Nile red in DMSO (Sigma-Aldrich) for 10 min at 25 °C in the dark [28, 29]. The stained neutral lipid droplets were observed with an Olympus BX53F2 upright optical microscope in epifluorescence mode, using a 130 W U-HGLGPS excitation source, TRITC filter, and  $\times 100$  (1.4 NA) Olympus oil-immersion objective. For each growth condition, about

100 cells were imaged with an Olympus DP74 camera. Using an image processing software, Fiji (ImageJ), each cell was selected individually with a custom-made program, and the raw fluorescence intensity of the Nile red-stained lipid droplets was measured for the selected cells.

## Data Analysis

### Multivariate Analysis of Micro-RS Data

Principal component analysis (PCA), statistical and ratio-metric analysis of Raman peak intensities for lipid C–C, C=C, and C=O stretching and  $\text{CH}_2/\text{CH}_3$  scissoring modes were performed using MATLAB R2015a. MATLAB was also used to generate normalized histograms of peak intensities to obtain the probability distribution of these quantities. Pearson's correlation coefficient was calculated among the cellular components starch, protein, carotenoid, chlorophyll, and saturated and unsaturated lipids and the correlation matrix was constructed using the customized Python codes. The coefficients were calculated for Raman spectra obtained from  $\sim 30$  individual cells.

To analyze heterogeneity in Raman peak centers and intensity across a population, the odds ratio (OR) was calculated using Eq. 2 for different stress conditions on day 6 and day 10 relative to the control culture on day 6.

$$\text{OR} = \frac{f_c/(1-f_c)}{f_s/(1-f_s)} = \frac{f_c(1-f_s)}{f_s(1-f_c)} \quad (2)$$

In the above equation, OR is calculated for a particular Raman mode, with  $f_c$  = the fraction of population of the control culture at day 6 with Raman peak center same as the median peak center,  $(1-f_c)$  = the fraction of population of the control culture at day 6 with Raman peak centers different from the median value of the population,  $f_s$  = fraction of population in a particular stress condition with Raman peak centers same as the population-scale median value,  $(1-f_s)$  = fraction of population in a particular stress condition with Raman peak centers different from the population-scale median value. Since OR quantifies heterogeneities relative to a control, this is referred to as the heterogeneity index (HI).

### Fatty Acid Analysis for Predicting Biofuel Properties

The degree of unsaturation (DU) present in the fatty acid (FA) content of the cell was calculated as the ratio of Raman peak intensity of  $\nu(\text{C}=\text{C})$  and  $\alpha(\text{CH}_2/\text{CH}_3)$  Raman modes ( $I_\alpha = I_{\nu(\text{C}=\text{C})}/I_{\alpha(\text{CH}_2/\text{CH}_3)}$ ). Biofuel parameters like cetane number (CN) [30], iodine value (IV, mg  $I_2$  absorbed per 100 g of oil), and higher heating value (HHV, MJ  $\text{kg}^{-1}$ ) were also calculated from the degree of unsaturation [31]. Additionally,

the fraction of SFA (saturated fatty acid) and UFA (unsaturated fatty acid) was also determined [32]. These calculations were run on three independent biological replicates. Error bars represent the standard deviation. The equations are as below:

$$\text{Cetane number (CN)} = 62.32 - 6.13 \times \text{DU} \quad (3)$$

$$\text{Iodine value (IV)} = 12.71 + 74.37 \times \text{DU} \quad (4)$$

$$\text{Higher heating value (HHV)} = 38.53 + 1.76 \times \text{DU} \quad (5)$$

Glyceryl trioleate was procured from Sigma-Y0001113 (referred to in the text as Triolein) and was used as a standard without further purification. Biofuel extracted from *Chlorella variabilis* (ATCC-PTA 12198) [33, 34] which has already been tested and found to efficiently run vehicles (referred to as MA Oil) was used for comparison with the biofuel properties of lipids tested in *C. reinhardtii*.

## Results

### Impact of Two-Stage Salt Stress on Growth and Cellular Morphology

In the line of experiments, the first focus was to check the effect of single-stage and two-stage salt stress on growth of *C. reinhardtii*. The growth curve of single-stage salt stress and two-stage salt stress is same as that of the control (Fig. 1B). It was observed that single-stage salt stress results in the palmelloid formation (Fig. 1C) wherein the cells gather in the group of 4 or more, surrounded by the extracellular matrix to combat against the stressful environment. Interestingly, this kind of morphological change was not observed in case of two-stage stress. Both D2 100 and D4 100 show no palmelloid development, when observed in the microscope. These results combinedly show that 100 mM NaCl induces the harmful effects of salt stress to only a limited extent and causes no significant change to the growth profile of *C. reinhardtii* cultures.

### Assignment of Raman Modes to Cellular Biomolecules

To study the effect of salt stress on microalgal growth and lipid composition and heterogeneity, micro-Raman spectra were acquired from ~30 individual cells belonging to each of the culture conditions as mentioned in the “Experimental Section.” Raman signal collected from a single microalgal cell with a short acquisition time is usually very weak, due to scattering and absorption of the incident beam by the cytoplasmic matrix, extracellular

media, pigments, or components of the cell wall. Moreover, cellular auto-fluorescence can result in a large non-uniform background too [16]. As a result of these factors, the Raman scattered signal obtained from the cells is noisy, with a large, variable background. After appropriate background subtraction and normalization (“Experimental Section”), a discrete wavelet transform (DWT) approach to denoise the noisy pre-treated data acquired for 2 s was found to yield reproducible peak positions and centers. This was cross-verified with Raman signals from each of the microalgal samples grown at different conditions and with the Raman data collected with 50 s accumulation time (data not shown). At this large accumulation time, even though noise is minimized due to signal averaging and whole-cell spectra can be obtained, long exposure to high laser power can alter the cellular dynamics resulting in erroneous results. Nevertheless, it gives a good estimate of the actual peaks present, which are deconvoluted with a Voigt function and peak centers accurately obtained. A drawback of this DWT denoising algorithm is that the data are down sampled, but this did not obscure the signal integrity and accuracy of the main Raman peaks considered in this study (Fig. S3). The DWT processed data were normalized for the strongest Raman peak (at around  $1523 \text{ cm}^{-1}$  corresponding to carotenoids) for each Raman data of the biological replicates for control (no stress), SS 100 (single-stage, 100 mM NaCl stress), D2 100 (two-stage, 100 mM NaCl added on the 2nd day of growth), and D4 100 (two-stage, 100 mM NaCl added on the 4th day), all acquired on the 6th day (end-log phase) (Fig. 2A). Raman signal acquired with 2 s acquisition time and subsequently DWT treated illustrated enhanced accuracy in the peak center estimates after the DWT treatment (Fig. S4). The normalized Raman signal was then used to analyze the fingerprint region in the wavenumber range of  $850\text{--}1800 \text{ cm}^{-1}$ , which revealed resolved contributions from various cellular constituents, such as photosynthetic pigments (chlorophyll and carotenoids), starch, proteins, and lipids. These peaks were deconvoluted with Voigt functions to obtain peak centers of the Raman bands chosen for study (Fig. 2B–F). The peaks identified after the transformation of Raman spectra with the DWT denoising algorithm accurately match previous estimates of Raman peaks observed for the biomolecules under study [35–37] as well as for *Chlamydomonas* sp. [14] (Table 1). The highest intensity peaks were assigned to carotenoids, specifically  $\beta$ -carotene (the in-plane  $\nu(\text{C}=\text{C})$  stretch at  $1156 \text{ cm}^{-1}$  and  $\nu(\text{C}=\text{C})$  stretching mode at  $1523 \text{ cm}^{-1}$ ), followed by chlorophyll peak at  $1288 \text{ cm}^{-1}$ , starch peak at  $864 \text{ cm}^{-1}$ , lipid peaks at 1063, 1086, 1440, 1656, and  $1750 \text{ cm}^{-1}$ , and proteins at  $1349 \text{ cm}^{-1}$ . In the following sections, Raman modes around these wavenumbers are further explored across individual cells.

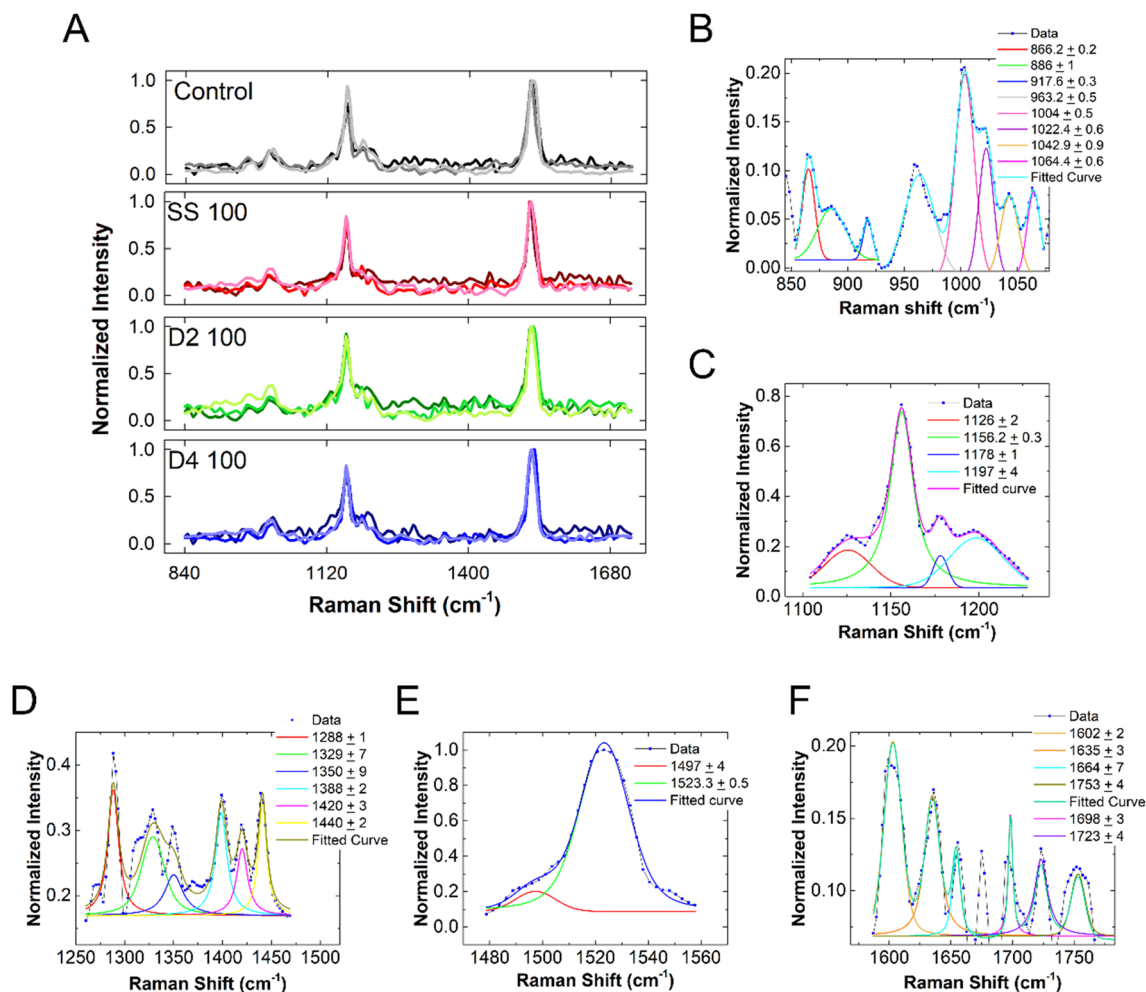


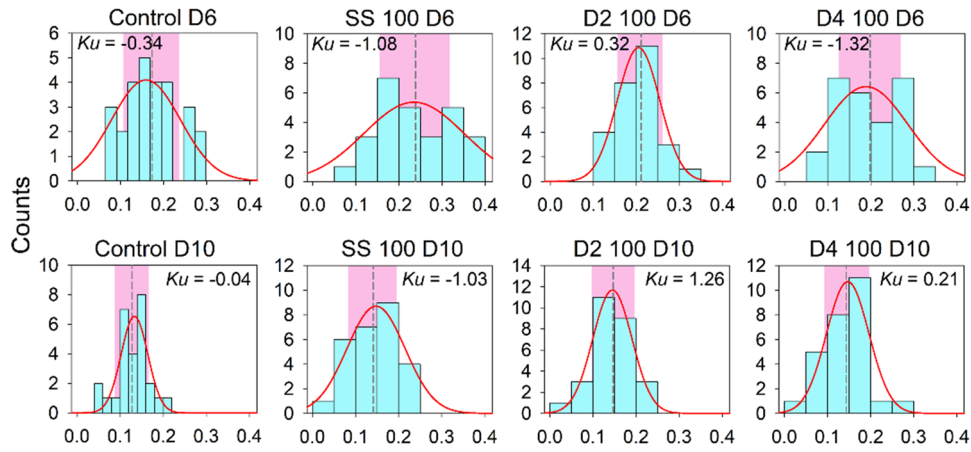
**Fig. 2** Deconvolution of the Raman spectra of *C. reinhardtii* cells yields distinct Raman peaks. **A** Overlay of DWT-treated Raman spectra across three biological replicates each of control (no NaCl), SS 100 (100 mM NaCl added on day 0), D2 100 (100 mM NaCl added on day 2), and D4 100 (100 mM NaCl added on day 4 of culture) captured on day 6 of growth. The Raman spectra obtained for

day 10 samples were similar to those of day 6 and hence not shown here to avoid repetition. Deconvolution and fitting of the smoothed Raman spectra using the Voigt function reveal distinct peaks used in the following study, viz., 866  $\text{cm}^{-1}$  and 1064  $\text{cm}^{-1}$  (**B**), 1156  $\text{cm}^{-1}$  (**C**), 1288, 1350 and 1440  $\text{cm}^{-1}$  (**D**), 1523  $\text{cm}^{-1}$  (**E**), and 1664 and 1753  $\text{cm}^{-1}$  (**F**)

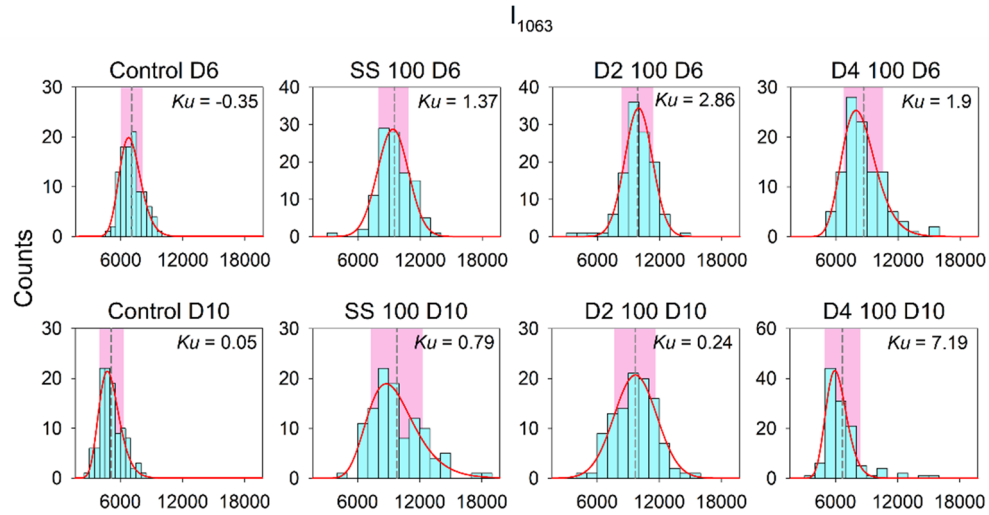
**Table 1** Raman peak assignments of starch, protein, chlorophyll, carotenoid, and lipids for *C. reinhardtii*

Wavenumber ( $\text{cm}^{-1}$ )	Component	Peak assignment	Reference
~864	Starch	C–O–C stretching and ring breathing modes in amylopectin and amylose units of starch	[14, 36]
1350	Protein	C–C $\alpha$ –H bending and C $\alpha$ –C stretching in $\alpha$ -helix or amide I and III regions of tryptophan	[37]
~1156	Photosynthetic pigments	In-plane stretching of C–C and deformation of C–H bonds in $\beta$ -carotene	[50]
~1288		Deformation of C–H and in-plane stretching of N–C bond in chlorophyll <i>a</i>	
~1523		In-plane stretching of C–C bond in $\beta$ -carotene	
~1064	Lipids	C–C stretching	[14, 35]
~1440		Scissoring of CH <sub>2</sub> /CH <sub>3</sub> bond	
~1656		C=C stretching	
~1750		C=O stretching	

**A**



**B**



**C**

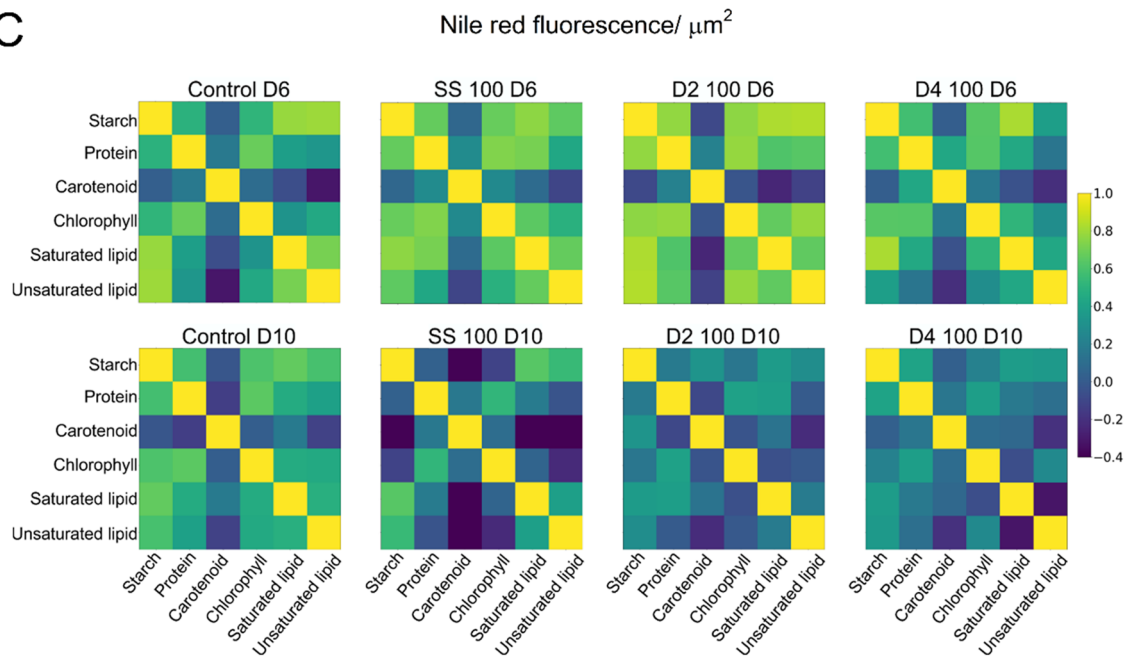




**Fig. 3** Validation and analysis of Raman bands of different biomolecules in *C. reinhardtii* cells under salt stress. **A** Distribution of lipid chain length measured by Raman spectroscopy at  $1063\text{ cm}^{-1}$  representing  $\nu(\text{C}=\text{C})_1$  vibration for  $\sim 30$  cells. **B** Probability distribution of Nile red fluorescence depicting neutral lipid droplets per area of the cell ( $\mu\text{m}^2$ ) measured for  $\sim 100$  cells. The red curve represents the fitted distribution. Gray-colored dashed line is the data average spanned on each side by the experimental standard deviation (highlighted with pink background).  $Ku$  is the kurtosis. **C** Pearson's correlation coefficients were calculated for cellular components—starch, protein, carotenoids, chlorophyll, saturated lipid, and unsaturated lipid for  $\sim 30$  cells each from the different cultivation conditions labeled at the top of each panel using the nomenclature mentioned in the text. Color scale ranges from yellow (correlation coefficient = 1, highest positive correlation, assigned for self-correlation) to blue (correlation coefficient =  $-0.4$ , highest negative correlation observed)

### Validation and Analysis of Raman Bands of Different Biomolecules in *C. reinhardtii* Cells Under Salt Stress

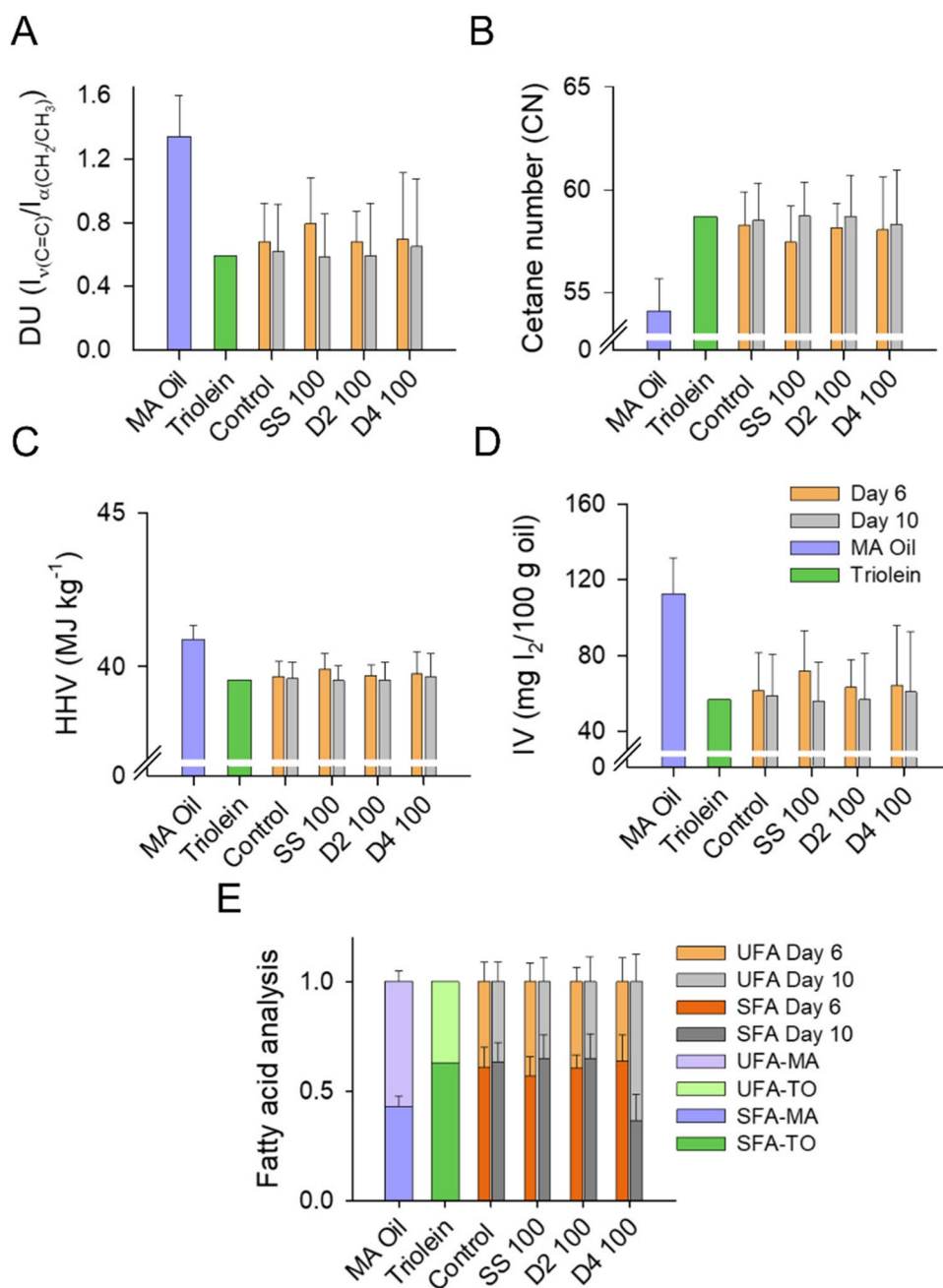
Raman laser spot size under the current experimental conditions is  $\sim 500\text{ nm}$ , which is  $1/20$ th part of the cell (*Chlamydomonas* is  $\sim 10\text{ }\mu\text{m}$  in diameter), rendering it a non-ideal representative of the absolute concentration of cellular bio-components. For this reason, the observed Raman intensities can only be used for relative measurements. Raman band at  $1063\text{ cm}^{-1}$  (C–C stretch of lipids) is first chosen to analyze lipids because the peak center of this band shows minimum fluctuations across different growth conditions (Fig. S5). This is compared to the absolute neutral lipid concentration in *C. reinhardtii* obtained from Nile red fluorescence intensity measurements by epifluorescence imaging of stained lipid droplets in about 100 cells and the fluorescence intensity per area of the cell estimated using Fiji software. The Raman intensity at  $1063\text{ cm}^{-1}$  is observed to be normally distributed for all growth conditions, like the single-cell Nile red fluorescence intensity distributions which fit to either normal or log-normal distributions (Fig. 3). Since the mean fluorescence intensity is a good measure of the lipid content of a cell, it is evident from Fig. 3B that lipid concentration increases in the presence of salt stress. The mean Raman intensities too show an increase in the different stress conditions compared to the control (Fig. 3A). In addition, the standard deviations, represented by the pink shaded region in each graph, also increase under stress as compared to control for both the Raman and Nile red fluorescence intensity distributions. Thus, in both cases, the distributions become more heterogeneous under salt stress. In both Raman and Nile red measurements, the distributions have similar kurtosis for control to start with, but show large deviations from the control culture distributions, especially in two-stage. Thus, even though Raman intensity is a poor indicator of the absolute biomolecule concentration, single-cell distributions can always be studied to shed light on the relative cellular changes imposed under stress.

Pearson's correlation matrix among cellular biocomponents, viz., starch, chlorophyll, carotenoids, and proteins along with lipids, was calculated using Raman intensities observed at wavenumbers mentioned in Table 1 and used in the previous analysis (Fig. 3C). Salt stress often imposes osmotic imbalance on the cell. The observations signify that  $100\text{ mM NaCl}$  added to the cultures is still below the threshold for such osmotic damage (Fig. 1B). Under such circumstances, it becomes essential to study the impact of salt stress on these cellular components. The correlation matrices show the overall negative correlations on day 10 in contrast to day 6. The correlation coefficients for the control culture remain unchanged over the growth cycle of the organism. Single-stage salt stress exhibits more negative correlations in comparison to two-stage cultures. Deteriorating correlation values on day 10 suggest poor growth in the stationary phase. There is a strong negative correlation between carotenoids-starch and carotenoids-lipid observed under all conditions. Chlorophyll-starch and chlorophyll-lipids are the correlations that become more negative under salt stress on day 10. This is also accompanied by hampered protein-lipid and starch-lipid inter-relations, the former being more pronounced in the single-stage while the latter in the two-stage. Noting that these correlation coefficients are mere indicators of a possible juggle between these biomarkers at a small fraction of the cell, these results denote how the bio-interplay is disturbed under salt stress and varies as a function of the mode of salt stress application. Thus, the results strongly demonstrate that Raman intensity correlations are sensitive to the age and salt stress condition of the culture and can be a rapid assay to determine the physiological state of cells under stress relative to an appropriate control.

### Biofuel Quality from Lipids Produced by *C. reinhardtii* Under Salt Stress

In the biofuel industry, increasing lipid productivity and producing biofuel of commercial quality are among the most essential requirements for maximizing profit. Biofuel quality is determined by the length of the carbon chain and degree of unsaturation (DU) of FAs, which decide the cetane number (CN). The average DU values for different culture conditions were calculated with ratiometric analysis, as the ratio of Raman peak intensity at C=C stretching ( $I_{\nu(\text{C}=\text{C})}$ , around  $1656\text{ cm}^{-1}$ ) to that of the  $\alpha\text{CH}_2/\text{CH}_3$  scissoring mode ( $I_{(\text{CH}_2/\text{CH}_3)}$ , around  $1440\text{ cm}^{-1}$ ). Using the micro-Raman signal in these lipid modes, the biofuel quality parameters of lipids produced by *C. reinhardtii* under salt stress were calculated using the formulae described in the experimental section. This analysis was performed on an ensemble of  $\sim 30$  cells and the population average values are shown in Fig. 4. Triolein (18:1C) and microalgal oil (MA Oil) extracted from CSMCRI's *Chlorella variabilis* were

**Fig. 4** Biofuel properties of lipids produced by *C. reinhardtii* under different modes of salt stress. Degree of unsaturation (A), cetane number (B), higher heating value (C), and iodine value (D). Fraction of saturated (SFA) and unsaturated fatty acid (UFA) in the population (E). Microalgal oil (MA Oil) extracted from *Chlorella variabilis* and processed for further use (see “Fatty Acid Analysis for Predicting Biofuel Properties”) and Triolein (TO) were used as standards. Values in plots are derived from three independent experiments, with error bars representing the standard deviation



used as standards (Raman spectra of MA Oil and Triolein are shown in Fig. S6). Interestingly, the average value of the parameters characterizing biofuel quality (Fig. 4) shows negligible variation for all the culture conditions under study. The average DU obtained for each condition was around 0.6 and the corresponding cetane number (CN) was found to be ~58 (Fig. 4A and B). The higher heating value (HHV) was found to be around  $40\ MJ\ kg^{-1}$  and iodine value (IV) in the range of 60–80  $mg\ I_2/100\ g\ oil$  (Fig. 4C, D). The fraction of saturated FAs is higher than the unsaturated FAs in all the conditions (Fig. 4E). Interestingly, all the biofuel parameters predicted here show similarity to the standard

Triolein, which is a mono-unsaturated 18C long-chain FA containing TAG.

Although the lipids produced by *C. reinhardtii* CC-125 under both single-stage and two-stage salt stress conditions were found to yield good biofuel quality, the notable indifference in composition demands an explanation of the impact of salt stress. Ideally, lipid composition can differ for different cells within a culture, and average values do not reveal these hidden heterogeneities in the lipid profile caused by different cell types of a population. Hence, simple averages of cellular response to stressful environments are not suitable parameters to understand the overall population-level

response. The significant indifference observed in the population means values of lipid profile upon exposure to salt stress entails an exploration of the response of individual cells in a population for detection of subpopulations with stress response different from the average behavior. The presence of these subpopulations cannot be overlooked because any stress condition which leads to an enhancement in these subpopulations can cause variations in biofuel quality. The goal of the two subsequent sections is therefore to analyze the presence of heterogeneities in lipid composition.

### Population-Scale Heterogeneities in Fatty Acid Chain Length in *C. reinhardtii* Grown Under Salt Stress

Capitalizing on the fact that micro-RS is an efficient tool to carry out high-resolution single-cell studies, lipid composition was explored across individual cells of a single culture. Lipid molecules are characterized by the number of carbon atoms (chain length) present in the FAs and the number of double bonds (degree of unsaturation) defined by the presence of C–C and C=C bonds, respectively. TAGs or triacylglycerol have three FAs esterified to a glycerol molecule, resulting in three C=O bonds and CH<sub>2</sub>/CH<sub>3</sub> groups in the FA chain. By analyzing the Raman spectra of several FA methyl esters of different chain lengths, Beattie

et al. have correlated the FA chain length to the ratio of the CH<sub>2</sub>/CH<sub>3</sub> scissoring mode ( $I_{\alpha}$ ) observed around 1440 cm<sup>-1</sup> and the C=O stretching mode around 1750 cm<sup>-1</sup> [38]. To study this aspect in the present Raman data, normalized histograms were generated for the ratio of peak intensity at 1440 cm<sup>-1</sup> to 1750 cm<sup>-1</sup> ( $I_{\alpha(\text{CH}_2/\text{CH}_3)}/I_{\text{C=O}}$ , referred to as  $I_{\beta}$ , Fig. 5) for different culture conditions at day 6 and day 10. The histograms could be fitted by the normal distribution function, with some outliers falling at the tails. Broad distribution curves show the presence of cellular diversity, especially for D2 100 D6, D4 100 D6, and D10. Outliers were observed in the probability distributions of the  $I_{\beta}$  ratio for the different culture conditions to get enhanced in salt stress conditions, demonstrating the presence of substantial cells that respond differently to salt stress in comparison to the average behavior. Overall, the diversity in FA chain length tends to vary under different types of salt stress applications. Further, the mean values obtained from the distribution dictate the average chain length of FA produced in the culture. These values (Fig. 5 caption) suggest an overall chain-shortening effect in D4 100, both at D6 and D10. Among the three types of salt stress, the two-stage stress D2 100 is more likely to produce long-chain length FAs and D4 100 to produce short-chain FAs throughout the growth of the culture. This analysis shows that salt stress increases heterogeneity in the FA chain

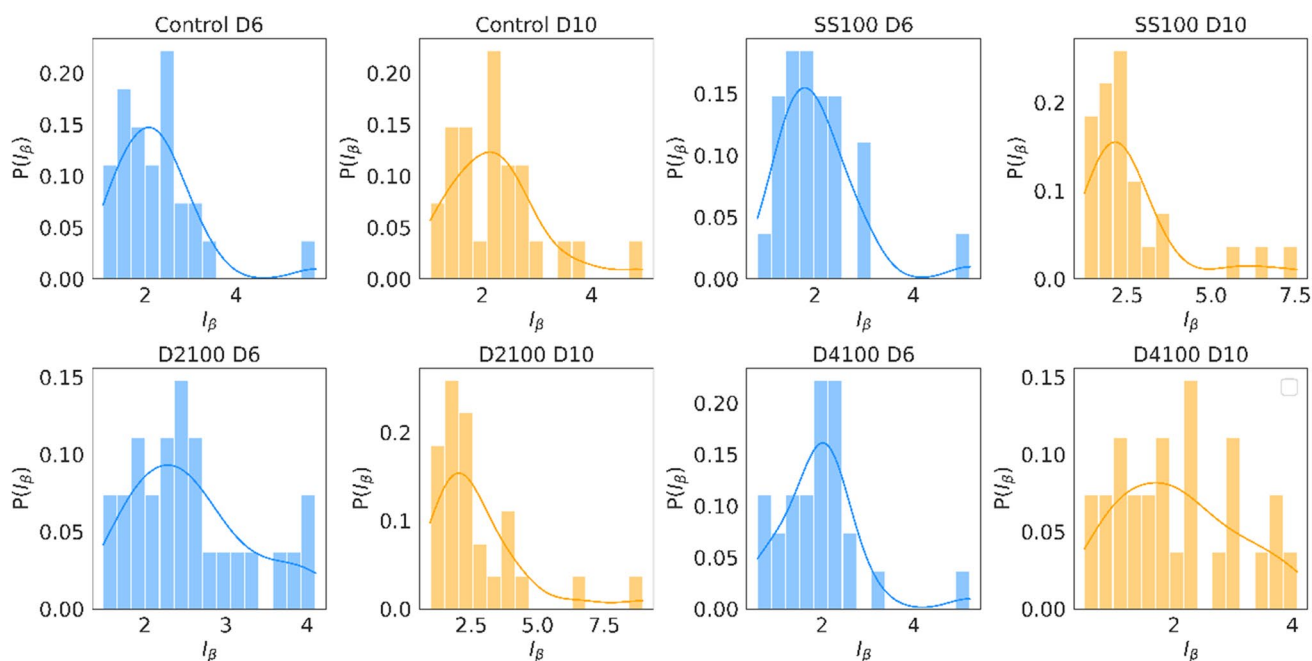


**Fig. 5** Probability distribution of the ratio of  $I_{\alpha(\text{CH}_2/\text{CH}_3)}$  and  $I_{\text{C=O}}$  ( $I_{\beta}$ ), as a function of incubation time and mode of application of salt stress in *C. reinhardtii*. Here,  $P(I_{\beta})$  represents the probability of occurrence of the peak intensity ratio  $I_{\beta}$  in the population. The mean values of the  $I_{\beta}$  ratio obtained from the distribution fit (shown by the solid

spline curve, blue for D6 and orange for D10) are 2.24 for control D6, 2.04 for control D10, 2.04 for SS 100 D6, 2.47 for SS 100 D10, 2.25 for D2 100 D6, 2.5 for D2 100 D10, 1.95 for D4 100 D6, and 1.73 for D4 100 D10

length. The heterogeneity further depends on how the salt stress is applied to the growing microalgal culture.

### Effect of Salt Stress on the Degree of Unsaturation of Lipids Produced by *C. reinhardtii*

The previously described validation analysis demonstrates that the unsaturation content of FAs in TAGs is an important criterion that governs biofuel quality. Hence, apart from analyses of heterogeneities in the chain length of FAs (Fig. 5), it is necessary to analyze variation in the *C. reinhardtii* population for the unsaturation content of TAGs. The unsaturation content in lipids can be calculated as a ratio of  $\nu(\text{C}=\text{C})$  mode around  $1656\text{ cm}^{-1}$ , to the  $\alpha(\text{CH}_2/\text{CH}_3)$  scissoring mode around  $1440\text{ cm}^{-1}$ . The Raman intensities at these wavenumbers show a significant peak formation (Fig. S7). A summary statistic of peak centers corresponding to the above modes for cultures grown under different conditions reveals substantial variability in the peak center values of the  $\alpha(\text{CH}_2/\text{CH}_3)$  and  $\nu(\text{C}=\text{C})$  modes (Fig. 6A–D). This variability is characterized by heterogeneity indices (HI) estimated from the OR values calculated using Eq. 2. Overall, heterogeneity observed in the  $\alpha(\text{CH}_2/\text{CH}_3)$  scissoring mode is less compared to other peaks studied so far. Most of the cells in the population for all the culture conditions studied have peak center values at  $1439\text{ cm}^{-1}$  or  $1440\text{ cm}^{-1}$ , except D2 100 at D6 which has most cells with a peak center at  $1442\text{ cm}^{-1}$  (Fig. 6A). For this mode, the HI values at D10 are very high, especially for single-stage SS 100, implying enhanced heterogeneity at the stationary growth phase (Fig. 6B).

In the case of the  $\nu(\text{C}=\text{C})$  mode distribution (Fig. 6C), the peak center is mostly observed at  $1655\text{ cm}^{-1}$  and  $1656\text{ cm}^{-1}$  for the control culture at D6 and D10, respectively. The HI values (Fig. 6D) are low in control, but there are outliers. These outliers cannot be neglected and result in broadening of the distribution when salt stress is applied, causing variability in the cellular stress response. Under both single and two-stage salt stress, the HI value increases at D10 (Fig. 6D). However, D4 100 has the highest heterogeneity both at D6 and D10, implying the production of lipids with a wide range of unsaturation (Fig. 6C, D). Thus, salt stress increases the heterogeneity in the unsaturation content, with maximum HI observed in two-stage, D4 100. This heterogeneity is also enhanced as the culture ages.

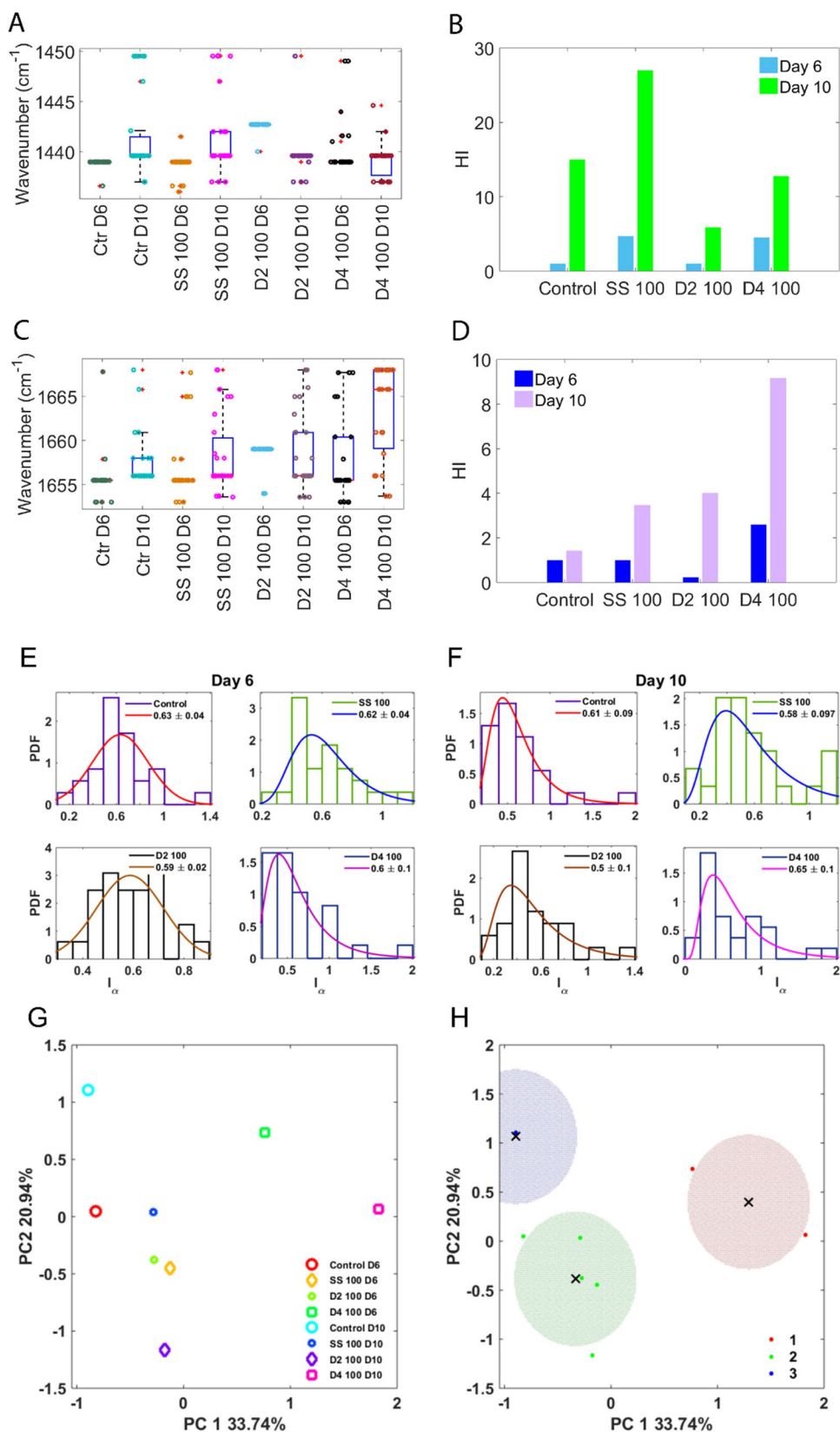
Further, the distribution of the degree of unsaturation (DU) in lipids under salt stress was characterized by carrying out a ratiometric analysis of the Raman peaks at olefinic  $\nu(\text{C}=\text{C})$  stretch which is around  $1656\text{ cm}^{-1}$  to the  $\alpha(\text{CH}_2/\text{CH}_3)$  peak around  $1440\text{ cm}^{-1}$ , referred to as  $I_\alpha$ . Probability density function (PDF), which gives the relative likelihood of the occurrence of the random variable  $I_\alpha$ , for  $\sim 30$  *C. reinhardtii* cells for each culture condition was obtained

(Fig. 6E, F). Symmetrical  $I_\alpha$  distributions were observed to be represented well by the normal distribution for all the D6 cultures except the stress condition D4 100 (Fig. 6E). At D10, the distributions become skewed and asymmetric with larger standard deviations (for D4 100 this is observed both at D6 and D10, Fig. 6F) and are better described by log-normal function. Overall, a large spread in the  $I_\alpha$  values illustrating population-scale heterogeneity in lipid DU was observed. Mean  $I_\alpha$  values calculated from these distributions are found to be around 0.6 in all cases (same as obtained in Fig. 4). The DU distribution for lipids of the D4 100 culture has higher unsaturation degree tails, which is observed to extend to a maximum value of 2, corresponding to 3 C=C bonds (tri-unsaturation) irrespective of the culture age [35]. On the other hand, SS 100 and D2 100 show the prevalence of cellular populations with maximum DU of 1.5–2.0 toward the stationary phase only same as the control, signifying the presence of bi-unsaturated lipids (2 C=C bonds) and tri-unsaturated lipids (3 C=C bonds) at D10, respectively. Thus, different culture conditions have cells that produce lipids with a reasonably wide spectrum of DU values (ranging from mono to tri-unsaturation), stressing the fact that the average DU values of around 0.6 (corresponding to mono-unsaturation) do not represent the entire population. The inherent heterogeneity in DU present in a population gets more randomized with stress and time. Therefore, like the heterogeneity observed in the FA chain length, the DU distributions also demonstrate that heterogeneity increases with the age of the culture, and D4 100 shows maximum variability throughout the culture. Further, the cultivation conditions were grouped together and divided into different clusters based on the degree of unsaturation obtained from the above analysis using principal component analysis (Fig. 6G, H). Three types of clusters were obtained in the analysis (Fig. 6H). Most of the cultivation conditions were clustered together except control D10 being an outlier (purple cluster, Fig. 6H) and D4 100 D6 and D10 forming the other cluster (red cluster, Fig. 6H). This further justifies that two-stage salt, D4 100, behaves differently than the other cultivation conditions under study and has great impact on the population-scale heterogeneity of the degree of unsaturation of lipids.

## Discussion

Raman spectroscopy-based techniques such as micro-RS and surface-enhanced Raman scattering (SERS) have become reasonably established methods for label-free, non-invasive, multiplexed detection of cellular biomolecules with good temporal as well as spatial resolution. The focus of this study is to understand the single-cell heterogeneities in lipid composition under different modes of salt stress applied

**Fig. 6** Effect of salt stress on the degree of unsaturation of lipids produced by *C. reinhardtii*. **A, C** Probability distribution of the  $\alpha(\text{CH}_2/\text{CH}_3)$  scissoring mode and  $\text{C}=\text{C}$  stretching mode, respectively, for the different salt stress treatments. The central red line in the box plots indicates the median, and the bottom and top edges of the box indicate the 25th and 75th percentiles, respectively. The whiskers extend to the most extreme data points not considered outliers, and the red “+” symbol represents outliers. **B, D** The heterogeneity index (HI) of the distributions of the  $\alpha(\text{CH}_2/\text{CH}_3)$  scissoring mode and  $\text{C}=\text{C}$  stretching mode, respectively, at both D6 and D10. Nomenclature for the culture conditions remains the same as depicted in Fig. 1. **E** Probability density functions (PDF) of DU at D6, mostly fitted well by normal distribution except the condition D4 100 (SS 100 histogram is fitted well by both normal and log-normal distribution). **F** Probability density functions of DU for D10, represented well by a log-normal distribution. The mean of the distribution obtained from the fitted curves is shown in each figure. **G** A principal component analysis of the degree of unsaturation studied for different growth conditions. **H** Cluster analysis depicting three clusters of similar variability between D4 100 D6 and D4 100 D10 (cluster 1, red), control D6, SS 100 D6, D2 100 D6, SS 100 D10, and D2 100 D10 (cluster 2, green), and control D10 (cluster 3, blue)



to *C. reinhardtii*, using micro-Raman spectroscopy. Discrete wavelet transform algorithm (DWT) was successfully employed to extract the spectral information in parallel to maintaining the essential signal integrity and accuracy with a good signal-to-noise ratio (Fig. 2). This method is more economical compared to high-resolution probes like SERS. In a recent study, SERS was used for single-cell lipid profiling to reveal the degree of unsaturation of lipids for *Scenedesmus quadricauda* grown under nutrient ( $N_2$ ) deprivation [39]. Similarly, the heterogeneities in lipid unsaturation and chain length were quantified using micro-RS. When discussing heterogeneities, it is an absolute requirement to confirm that it is not just an artifact but a genuine representation of the cell's metabolite picture. It is important to note that here only a small fraction (1/20th) of a *C. reinhardtii* cell was explored, and the presence of a particular biomolecule in the focus is detected with the help of the characteristic fingerprint Raman spectrum. Bright field and fluorescence microscopy shows that chlorophyll and lipid droplets are distributed in a large area of the cell (Fig. 1). Lipid droplets are shown to be distributed in the cytosol [40]. Starch, too, is either distributed in the cup-shaped chloroplast stroma or can be found surrounding the pyrenoids [41]. Thus, the probability of capturing the biomolecules under consideration in the focal point is highly likely. In this study, Raman spectroscopy data yield only relative scale measurements of stress, where they reveal a disintegrating cellular stasis on day 10 (Fig. 3), especially under salt stress. For absolute quantification of lipids in this study, Nile red fluorescence shows an increase in lipid content in *C. reinhardtii* cells under salt stress (Fig. 3). It also shows that the distribution becomes more heterogeneous under stress, which is also a key feature of Raman intensity measurements. Although absolute quantification is not possible by the method presented here, biomolecular Raman intensities are able to detect biomolecule chemical composition of a microalgal cell.

Using the Raman spectral information of the lipid molecules, salt stress was found to lead lipid production of good biofuel quality in *C. reinhardtii* (Fig. 4). The higher heating value (HHV) and iodine value (IV) were found to conform with the European standards of biofuel quality [30, 42] as well as the Indian diesel specifications enumerated by the Ministry of Road Transport and Highways (MoRTH) and the Ministry of Petrol and Natural Gas (MoPNG). Moreover, the average unsaturation degree values (0.6) indicate the predominance of mono-unsaturated TAGs making the oil oxidative stable [31, 42]. These properties are observed to be well aligned with the standard Triolein (18:1). This analysis renders the suitability of Raman spectroscopy for efficient biofuel quality determination.

The average Raman data analysis shows that both single-stage and two-stage salt stress produce lipids with same biodiesel quality parameters, but single-cell heterogeneities

(measured by the heterogeneity index) were found to be higher in two-stage salt stress. Both fatty acid chain length and the unsaturation content were studied. Ratiometric intensity probability distribution analysis for  $I_{\alpha(CH_2/CH_3)}/I_{C=O}$  (Fig. 5) shows that shorter chain length FAs are produced more in two-stage D4 100. A possible reason for chain shortening here could be the activation of the  $\beta$ -oxidation pathway under stress [43], where enzymatic degradation of lipids takes place to release energy in the form of ATP. It can also be due to autophagy, a hint of which is evident in the correlation analysis (Fig. 3) as well as from the negative carotenoid and starch/lipid correlation [44]. Autophagy is a catabolic process and is activated to counterbalance the effect of stress on the cell by recycling the damaged material to maintain the cell's homeostasis [45]. Furthermore, ratiometric analysis of  $\nu(C=C)$  stretching mode to  $CH_2/CH_3$  scissoring mode reveals higher proportion of subpopulation exhibiting bi-tri-unsaturation in their fatty acids, especially on day 10 of D4 100 (Fig. 6). Thus, an overall increased heterogeneity in D4 100 shows that this strategy of salt stress exerts more variable metabolic options on the population. It can be said that each subpopulation could undergo different transcriptome and proteome development to explore the best possible mechanism of fitness [46].

The question which arises is what is the biological implication of this heterogeneity? It has been well documented that heterogeneous behavior is often induced when microbial cultures face environmental stress [47, 48]. Stress also means shortage of nutrient availability as the culture attains its stationary phase. Under such stressful conditions, subpopulations present inside one main population account for one of the population-level strategies for adaptation and evolution. Distributing the workload is one such evolution strategy that gives rise to single-cell heterogeneities. Raman spectroscopy-oriented heterogeneity studies allow to understand the possible responses of individual cells in a population and their coherent effort in population survival. Although culture synchronization aims to grow cells with maximum homogeneity, stress can induce heterogeneities with longer incubation time [18, 49]. The current study lacks culture synchronization methods, but the heterogeneity discussed is relative to the control grown under same conditions except the stress. Here, major source of heterogeneity could be either the varying lipid composition under salt stress or the fact that the laser beam is focused on different regions of the cell. In the latter case, the heterogeneity could arise due to spatial modulations of composition of biomolecules due to proximity of different organelles. A single-cell spatial Raman mapping for the entire cell volume could elucidate the exact reason of these heterogeneities. Recent studies have revealed the important role played by gene expression changes in regulating the lipid turnover under salinity stress and liquid-liquid phase separation of lipid droplets in *C.*

*reinhardtii* cells, which in turn contributes to the heterogeneous response to salinity stress [50]. Heterogeneity within a single culture is a significant technical concern during large-scale growth for industrial-scale biofuel production.

## Conclusions

With the help of heterogeneity indices obtained for the FA chain length and unsaturation content in the TAGs, this study on single-stage and two-stage salt stress detects the overlooked presence of subpopulations in a culture. This heterogeneity is maximum under two-stage cultivation and at the stationary growth phase. This study underlines the need for rapid optimization of stress conditions and harvest time for good biofuel quality with non-invasive tools like micro-Raman spectroscopy. Cellular heterogeneity can be a potential bottleneck for good lipid productivity of uniform quality.

**Supplementary Information** The online version contains supplementary material available at <https://doi.org/10.1007/s12155-024-10799-4>.

**Acknowledgements** SP, GA, and DB are very thankful to Dr. Sharad B. Pillai for help with the Raman experiments and Prof. G. Naresh Kumar for valuable discussions. SP gratefully acknowledges UGC for fellowship.

**Funding** This research received late-stage funding from GSBTM to D.B.; the micro-Raman spectrometer was procured with a DST-PURSE grant to the Faculty of Science.

**Data Availability** Data presented in this manuscript can be obtained from the corresponding author on reasonable request.

## Declarations

**Conflict of Interest** The authors declare no competing interests.

## References

- Demirbas A, Demirbas MF (2011) Importance of algae oil as a source of biodiesel. *Energy Convers Manag* 52(1):163–170. <https://doi.org/10.1016/j.enconman.2010.06.055>
- Kose A, Oncel SS (2017) Algae as a promising resource for biofuel industry: facts and challenges. *Int J Energy Res* 41(7):924–951. <https://doi.org/10.1002/er.3699>
- Behera S, Singh R, Arora R, Sharma NK, Shukla M, Kumar S (2015) Scope of algae as third generation biofuels. *Front Bioeng Biotechnol* 2:1–13. <https://doi.org/10.3389/fbioe.2014.00090>
- Stephens E, Ross IL, Mussgnug JH, Wagner LD, Borowitzka MA, Posten C, Kruse O, Hankamer B (2010) Future prospects of microalgal biofuel production systems. *Trends Plant Sci* 15(10):554–564. <https://doi.org/10.1016/j.tplants.2010.06.003>
- Cheng D, He Q (2014) Assessment of environmental stresses for enhanced microalgal biofuel production – an overview. *Front Energy Res* 2:1–8. <https://doi.org/10.3389/fenrg.2014.00026>
- Bazzani E, Lauritano C, Mangoni O, Bolinesi F, Saggiomo M (2021) *Chlamydomonas* responses to salinity stress and possible biotechnological exploitation. *J Mar Sci Eng* 9(11). <https://doi.org/10.3390/jmse9111242>
- Chu W (2017) Strategies to enhance production of microalgal biomass and lipids for biofuel feedstock. *Eur J Phycol* 52(4):419–437. <https://doi.org/10.1080/09670262.2017.1379100>
- Remmers IM, Hidalgo-Ulloa A, Brandt BP, Evers WAC, Wijffels RH, Lamers PP (2017) Continuous versus batch production of lipids in the microalgae *Acutodesmus obliquus*. *Bioresour Technol* 244:1384–1392. <https://doi.org/10.1016/j.biortech.2017.04.093>
- Nagappan S, Devendran S, Tsai PC, Dahms HU, Ponnusamy VK (2019) Potential of two-stage cultivation in microalgae biofuel production. *252(100):339–349*. <https://doi.org/10.1016/j.fuel.2019.04.138>
- Ho SH, Nakanishi A, Ye X, Chang JS, Hara K, Hasunuma T, Kondo A (2014) Optimizing biodiesel production in marine *Chlamydomonas* sp. JSC4 through metabolic profiling and an innovative salinity-gradient strategy. *Biotechnol Biofuels* 7(1):1–16. <https://doi.org/10.1186/1754-6834-7-97>
- Moser BR (2009) Biodiesel production, properties, and feedstocks. *Vitr Cell Dev Biol-Plant* 45(3):229–266. <https://doi.org/10.1007/s11627-009-9204-z>
- Challagulla V, Nayar S, Walsh K, Fabbro L (2016) Critical reviews in biotechnology advances in techniques for assessment of microalgal lipids. 8551:0–13. <https://doi.org/10.1080/07388551.2016.1206058>
- Cavonius L, Fink H, Kiskis J, Albers E, Undeland I, Enejder A (2015) Imaging of lipids in microalgae with coherent anti-Stokes Raman scattering microscopy. *Plant Physiol* 167(3):603–616. <https://doi.org/10.1104/pp.114.252197>
- He Y, Zhang P, Huang S, Wang T, Ji Y, Xu J (2017) Label-free, simultaneous quantification of starch, protein and triacylglycerol in single microalgal cells. 10:1–18. <https://doi.org/10.1186/s13068-017-0967-x>
- Baladehi MH, Hekmatara M, He Y, Bhaskar Y, Wang Z, Liu L, Ji Y, Xu J (2021) Culture-free identification and metabolic profiling of microalgal single cells via ensemble learning of ramanomes. *Anal Chem*. <https://doi.org/10.1021/acs.analchem.1c01015>
- Huang YY, Beal CM, Cai WW, Ruoff RS, Terentjev EM (2010) Micro-Raman spectroscopy of algae: composition analysis and fluorescence background behavior. *Biotechnol Bioeng* 105(5):889–898. <https://doi.org/10.1002/bit.22617>
- Da CL, Ho SH, Shimada R, Ren NQ, Ozawa T (2017) Rapid in vivo lipid/carbohydrate quantification of single microalgal cell by Raman spectral imaging to reveal salinity-induced starch-to-lipid shift. *Biotechnol Biofuels* 10(1):1–9. <https://doi.org/10.1186/s13068-016-0691-y>
- Wang T, Ji Y, Wang Y, Jia J, Li J, Huang S, Han D, Hu Q, Huang WE, Xu J (2014) Quantitative dynamics of triacylglycerol accumulation in microalgae populations at single-cell resolution revealed by Raman microspectroscopy. *Biotechnol Biofuels* 7(1):1–12. <https://doi.org/10.1186/1754-6834-7-58>
- Jaeger D, Pilger C, Hachmeister H, Oberländer E, Wördenweber R, Wichmann J, Mussgnug JH, Huser T, Kruse O (2016) Label-free in vivo analysis of intracellular lipid droplets in the oleaginous microalga *Monoraphidium neglectum* by coherent Raman scattering microscopy. *Sci Rep* 6(October):2–10. <https://doi.org/10.1038/srep35340>
- Wu H, Volponi JV, Oliver AE, Parikh AN, Simmons BA, Singh S (2011) In vivo lipidomics using single-cell Raman spectroscopy. *Proc Natl Acad Sci* 108(9):3809–3814. <https://doi.org/10.1073/pnas.1009043108>
- Wei X, Jie D, Cuello JJ, Johnson DJ, Qiu Z, He Y (2014) Trends in Analytical chemistry microalgal detection by Raman

- microspectroscopy. *Trends Anal Chem* 53:33–40. <https://doi.org/10.1016/j.trac.2013.09.012>
22. Altschuler SJ, Wu LF (2010) Cellular heterogeneity: do differences make a difference? *Cell* 141(4):559–563. <https://doi.org/10.1016/j.cell.2010.04.033>
  23. Balaban NQ, Merrin J, Chait R, Kowalik L, Leibler S (2004) Bacterial persistence as a phenotypic switch. *Science* 305(5690):1622–1625. <https://doi.org/10.1126/science.1099390>
  24. Elowitz MB, Levine AJ, Siggia ED, Swain PS (2002) Stochastic gene expression in a single cell. *Science* 297(5584):1183–1186. <https://doi.org/10.1126/science.1070919>
  25. Harris EH (2001) *Chlamydomonas* as a model organism. *Annu Rev Plant Physiol Plant Mol Biol* 52:363–406. <https://doi.org/10.1146/annurev.arplant.52.1.363>
  26. Atikij T, Syaputri Y, Iwahashi H, Praneenarat T, Sirisattha S, Kageyama H, Waditee-Sirisattha R (2019) Enhanced lipid production and molecular dynamics under salinity stress in green microalga *Chlamydomonas reinhardtii* (137C). *Mar Drugs* 17(8):2019. <https://doi.org/10.3390/md17080484>
  27. Pandey S, Archana G, Bagchi D (2022) Micro-Raman spectroscopy of the light-harvesting pigments in *Chlamydomonas reinhardtii* under salinity stress. *Spectrochim Acta - Part A Mol Biomol Spectrosc* 281:121613. <https://doi.org/10.1016/j.saa.2022.121613>
  28. Chen W, Zhang C, Song L, Sommerfeld M, Hu Q (2009) A high throughput Nile red method for quantitative measurement of neutral lipids in microalgae. *J Microbiol Methods* 77(1):41–47. <https://doi.org/10.1016/j.mimet.2009.01.001>
  29. Kou Z, Bei S, Sun J, Pan J (2013) Fluorescent measurement of lipid content in the model organism *Chlamydomonas reinhardtii*. *J Appl Phycol* 25(6):1633–1641. <https://doi.org/10.1007/s10811-013-0011-x>
  30. Sarakatsanis CK (2019) A comparative assessment of biodiesel cetane acid composition. *12(422):1–30*. <https://doi.org/10.3390/en12030422>
  31. Calixto CD, da Silva Santana JK, Tibúrcio VP, de Pontes L de FBL, da Costa Sassi CF, da Conceição MM, Sassi R (2018) Productivity and fuel quality parameters of lipids obtained from 12 species of microalgae from the northeastern region of Brazil. *Renew Energy* 115:1144–1152. <https://doi.org/10.1016/j.renene.2017.09.029>
  32. Elizabeth CE, Lakshmi PK, Meenakshi S, Vaidyanathan S, Srisudha S, Mary MB (2020) *Spectrochimica Acta Part A : Molecular and Biomolecular Spectroscopy* Biomolecular transitions and lipid accumulation in green microalgae monitored by FTIR and Raman analysis. *Spectrochim Acta Part A Mol Biomol Spectrosc* 224:117382. <https://doi.org/10.1016/j.saa.2019.117382>
  33. Ghosh PK, Mishra SC., Maiti S, Paliwal C, Mishra SK, Ghosh T, Patel P and Bharadia JN (2015) Solar driven solvent extractor and process for extraction of microalgal lipids using the same. *US 2015(0057459 A1):1–5*
  34. Bhattacharya S, Maurya R, Kumar S, Ghosh T (2016) Solar driven mass cultivation and the extraction of lipids from *Chlorella variabilis* : a case study. *Algal Res* 14:137–142. <https://doi.org/10.1016/j.algal.2016.01.009>
  35. Czamara K, Majzner K, Pacia MZ, Kochan K, Kaczor A, Baranska M (2015) Raman spectroscopy of lipids: a review. *J Raman Spectrosc* 46(1):4–20. <https://doi.org/10.1002/jrs.4607>
  36. Wiercigroch E, Szafraniec E, Czamara K, Pacia MZ, Majzner K and Kochan K (2017) SC. *Spectrochim Acta Part A Mol Biomol Spectrosc*. <https://doi.org/10.1016/j.saa.2017.05.045>.
  37. Rygula A, Majzner K, Marzec KM, Kaczor A, Pilarczyk M (2013) Raman spectroscopy of proteins : a review. *J Raman Spectrosc* 44(8):1061–1076. <https://doi.org/10.1002/jrs.4335>
  38. Beattie JR, Bell SEJ, Moss BW (2004) A critical evaluation of Raman spectroscopy for the analysis of lipids: fatty acid methyl esters. *Lipids* 39(5):407–419. <https://doi.org/10.1007/s11745-004-1245-z>
  39. Ramya AN, Ambily PS, Sujitha BS, Arumugam M, Kumar K (2017) Single cell lipid profiling of *Scenedesmus quadricauda* CASA-CC202 under nitrogen starved condition by surface enhanced Raman scattering (SERS) fingerprinting. *Algal Res* 25:200–206. <https://doi.org/10.1016/j.algal.2017.05.011>
  40. Li-Beisson Y, Kong F, Wang P, Lee Y, Kang BH (2021) The disassembly of lipid droplets in *Chlamydomonas*. *New Phytol* 231(4):1359–1364. <https://doi.org/10.1111/nph.17505>
  41. Busi M V., Barchiesi J, Martín M, Gomez-Casati DF (2014) Starch metabolism in green algae. *66(1–2):28–40*. <https://doi.org/10.1002/star.201200211>
  42. Giakoumis EG (2013) A statistical investigation of biodiesel physical and chemical properties, and their correlation with the degree of unsaturation. *Renew Energy* 50:858–878. <https://doi.org/10.1016/j.renene.2012.07.040>
  43. Kong F, Romero IT, Li-beisson Y, Warakanont J (2018) Lipid catabolism in microalgae. *New Phytol* 218:1340–1348. <https://doi.org/10.1111/nph.15047>
  44. Davey MP, Horst I, Duong GH, Tomsett EV, Litvinenko ACP, Howe CJ, Smith AG (2014) Triacylglyceride production and autophagous responses in *Chlamydomonas reinhardtii* depend on resource allocation and carbon source. *Eukaryot Cell* 13(3):392–400. <https://doi.org/10.1128/EC.00178-13>
  45. Couso I, Pérez-Pérez ME, Martínez-Force E, Kim H-S, He Y, Umen JG, Crespo JL, Bozhkov P (2017) Autophagic flux is required for the synthesis of triacylglycerols and ribosomal protein turnover in *Chlamydomonas*. *J Exp Bot*. <https://doi.org/10.1093/jxb/erx372>
  46. Cross FR, Umen JG (2015) The *Chlamydomonas* cell cycle. *Plant J* 82(3):370–392. <https://doi.org/10.1111/tpj.12795>
  47. Martins BMC, Locke JCW (2015) Microbial individuality: how single-cell heterogeneity enables population level strategies. *Curr Opin Microbiol* 24:104–112. <https://doi.org/10.1016/j.mib.2015.01.003>
  48. Lidstrom ME, Konopka MC (2010) The role of physiological heterogeneity in microbial population behavior. *Nat Chem Biol* 6(10):705–712. <https://doi.org/10.1038/nchembio.436>
  49. Tanay A, Regev A, Science C (2017) Scaling single-cell genomics from phenomenology to mechanism. *Nature* 541(7637):331–338. <https://doi.org/10.1038/nature21350.Single>
  50. Pandey S, Visavadiya P, Patil V et al (2024) Salinity stress-mediated lipid droplet production and liquid–liquid phase separation in *Chlamydomonas reinhardtii*. *Eur Phys J Spec Top*. <https://doi.org/10.1140/epjs/s11734-024-01186-3>

**Publisher's Note** Springer Nature remains neutral with regard to jurisdictional claims in published maps and institutional affiliations.

Springer Nature or its licensor (e.g. a society or other partner) holds exclusive rights to this article under a publishing agreement with the author(s) or other rightsholder(s); author self-archiving of the accepted manuscript version of this article is solely governed by the terms of such publishing agreement and applicable law.